

No-reference Image Blur Assessment and Blur Map Estimation based on Multiresolution DCT Features

Zheng Zhang, *Member, IEEE*, Xinhua Xiao, Hanlin Tan, Yu Liu, Maojun Zhang

Abstract—In this paper, we propose a new method of image blur assessment and we extend it for image blur detection. By analyzing the statistics of multiscale Local-Mean Magnitude (LMM) maps, which are constructed based on a multiresolution decomposition of DCT blocks, our method presents an effective model for quantifying image sharpness and for blur detection. This model is established via the combination of a set of inter-scale and inter-directional sharpness ratios computed on detected high-activity blocks, where the corresponding weighting parameters are adaptively determined. Our method also considers the model of change in the edge structures of multiscale directional edge maps. The image’s overall sharpness is computed as a weighted geometric mean combination of these models with a weighted log-energy sharpness index. This method has been evaluated on several public image databases and been shown to outperform the current state-of-the-art methods. Based the proposed model, we extend it for blur detection, and find it shows competitive performance on accurate blur map estimation.

Index Terms—No-Reference Image Sharpness Assessment, Blur Detection, Image Enhancement

I. INTRODUCTION

VARIOUS distortions occur in the pipeline of imaging, such as noise, blurring, blocking and ringing. If serious enough, these distortions would be visible to human viewers, and would tend to affect the perceptual quality of the image. Sharpness has a big influence on perceived image quality because it determines the degree of detail an image conveys. Besides being used for image quality assessment (IQA), measurement of image sharpness is also of fundamental importance for various applications, such as image enhancement [1], denoising [2], and deblurring [3].

In this paper, we are mainly concerned with no-reference (NR) image sharpness assessment. A NR method predicts the sharpness of an image without using any information of the original image. It is difficult to assess NR image sharpness accurately because many factors affect it, such as image content, spatial resolution, and contrast [4], [5]. By “accurate” we mean that the algorithm’s prediction should be in very close agreement with human judgments. Existing spatial edge-based methods [2], [6]–[12] offer some level of accuracy, but may not achieve consistent performance for images with high blur levels owing to their reliance on edge detection [7]. Various frequency-based algorithms [13]–[23] exploit the fact that blur is intrinsically caused by the attenuation of high frequencies, thus they mostly predict sharpness using a single model based on the frequency contents that change

with the attenuation of frequency. Recent frequency-based methods [20], [22], [23] have shown impressive improvement in performance. Greater accuracy may be even achieved by using hybrid approaches (*e.g.*, the S3 algorithm [5]) which combines both spatial and frequency models, or by exploiting the sharpness model based on the estimation of autoregressive (AR) parameters [24]. However, these models often rely on computing steps that have a high computational cost (*e.g.*, the block-wise model of total variation computation in [5], or the estimation of pixel-wise AR parameters [24]). This may restrict their use in applications where computational resources is limited.

In this work, we proposed a new NR sharpness assessment algorithm by using block DCT data. We focus on using DCT data because our algorithm is intended to be appropriate for DCT-based compressed video or images, where it can directly utilize the available DCT information. DCT has been widely used for image and video compression algorithms (*e.g.*, JPEG, MPEG2, H263, and H264). Besides, many optimized specific platforms and fast algorithms are available for DCT implementation [25], [26]. Our method first constructs multiple LMM maps based on a multiscale DCT decomposition. These LMM maps have structure similarity and capture image energy concentration at different scales and directions. By analyzing the distributions of standard deviation ratios between LMM maps, we found a set of inter-scale and inter-directional sharpness measures which are in close correlation with the blur level. To reduce the effect of smooth areas on sharpness assessment, high-activity blocks are detected using a simple activity measure with an adaptive detection rate. The linear combination of the sharpness ratios computed on detected high-activity blocks induces an effective sharpness model, where the weighting parameters are adaptively estimated. To enhance accuracy, sharpness factors based on the blur effect on DCT edges and log-energy are also incorporated into our method. The main characteristics and contributions of our algorithm are summarized below:

- We propose a new, effective sharpness model based on the statistical analysis of multiscale LMM maps. This model measures sharpness by utilizing a set of inter-scale and inter-directional sharpness measures computed on high-activity blocks and adjusting each part’s effect using automatic estimated weighting parameters
- In addition to the model already described, our method also considers the blur effect on edge structures and log-energy distributions, and presents an edge-structure based model and a log-energy based model. All models are

Z. Zhang, H. Xiao, H. Tan, Y. Liu and M. Zhang are with the College of System Engineering, National University of Defense Technology, China (*e-mail*: {zhangzheng, jasonyliu, zhxiong, huaxinxiao, mjzhang@nudt.edu.cn}).

- closely interconnected in our multiscale DCT framework.
- The proposed algorithm is computational efficient and has achieved a significant improvement in performance over state-of-the-art methods.

II. RELATED WORK

The vast majority of existing NR sharpness assessment algorithms generally use models to quantify the strengths of edge. Examples of early edge-based techniques include measuring edge width [6], [7] or using edge gradient [8], [9]. Ferzli and Karam proposed a novel edge based metric by incorporating a concept of just noticeable blur (JNB) into a probability summation model. Inspired by this approach, the method [12] predicts image sharpness by computing the cumulative probability of blur detection at each edge. The recent work [27] introduced an efficient perceptual sharpness index, which is based on the incorporation of perceptual properties with statistical edge features. Recent investigations [27], [28] have shown that using statistical edge features [27] or local variance [28] may improve the performance of these spatial-based techniques.

Another research line is to perform sharpness assessment in the frequency domain. One early method is proposed in [13], where the slope of the amplitude spectrum is exploited to predict perceived blur. This method is motivated by the fact that the falling of the amplitude spectrum of a natural sharp image generally obeys a law, but when blur occurs, the spectrum falls faster than the original image. Because blur reduces the high-frequency energy associated with edges and fine details, several sharpness models have been proposed. Marichal *et al.* [14] suggest using the histogram of non-zero coefficients in DCT blocks. Tong *et al.* considered the percentage of wavelet transform edges that lose sharpness because of the blur effect. Shaked and Tastl [16] exploit localized frequency content analysis in a feature-based context. Caviedes and Oberti [15] use 2D kurtosis of 8×8 DCT combined with edge detection. In recent years, several frequency-based metrics have achieved high levels of sharpness prediction [20], [22], [23]. The work [20] presents a fast image sharpness measure using a weighted average of log-energies of three-level discrete wavelet transform. In a similar multiscale framework, the metric [23] estimates blurriness using DCT edges. Another recent metric is presented in [22], which identifies sharpness as strong LPC near distinctive image features with complex wavelet transform.

All the aforementioned methods assesses sharpness using a single model either in the frequency or the spatial space. A useful idea is to exploit multiple models to measure sharpness from different ways and then obtain an overall estimate via a pooling or weighting step. One example is the recent S3 algorithm [5] which combines a power spectral based model and a spatial local variation model. Another example is the very recent AR-based image sharpness metric (ARISM) proposed in [24]. This method works in AR space, and measures sharpness by combining a contrast-based measure and energy-based measure with AR parameter estimation. Our method falls in this multimodel framework, where we exploits

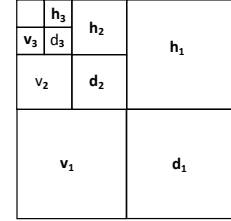


Fig. 1. Every 8×8 DCT block is taken as three-scale tree structure with ten-subband decomposition, where the subbands h_i , v_i and d_i form the i -th scale.

block-based models in the DCT domain. Compared with these current-state-of-the-art multimodel-based techniques, our method outperforms them both in accuracy and efficiency.

III. NO-REFERENCE SHARPNESS ASSESSMENT

A. Multiscale Local-Mean Magnitude Maps

Our sharpness metric is in the DCT domain. Given an input image to be evaluated, we first divide it into non-overlapping 8×8 blocks and then transfer each block to the DCT domain. The use of non-overlapping 8×8 blocks makes our metric well suited for compressed video or images where 8×8 DCT blocks are often already available. In our method, every DCT block is taken as three-scale tree structure with ten-subband decomposition. Fig. 1 illustrates this multiscale decomposition, where h_i , v_i and d_i separately denote the horizontal, vertical, and diagonal subbands at the i -th scale ($i = 1, 2, 3$). This form of decomposition has been used in algorithms for image compression [29], [30], IQA [31] and image blurriness estimation [23]. With this multiscale decomposition, multiple LMM maps can be built from the entire image. LMM here is defined as the average magnitude of coefficients in a subband, hence 1 block gives 9 LMM feature points. Each LMM feature point of the subbands with the same type and index from all blocks are grouped and put onto their corresponding positions to form a LMM map. For the entire image, we then obtain a total of 9 LMM maps of the same size. For clarity, let H_i , V_i and D_i denotes the LMM maps correspond to the three types of subbands h_i , v_i and d_i separately ($i = 1, 2, 3$). Fig. 2 illustrates the multiscale LMM maps of the original Lena image and its blurred version. From this figure, the following may be seen:

- (1) Structure similarity between LMM maps and magnitude decay across LMM maps can be observed; more image energy is compacted into the subbands of higher scales or lower frequency;
- (2) Blur affects image sharpness at different scales and reduces image energy across subbands; subbands of lower scale or higher frequency would be more easily affected by blur;
- (3) Subbands at the same scale shows differences in energy concentration and a directional distribution of coefficients;

Our method exploits these observations to develop a new sharpness model.

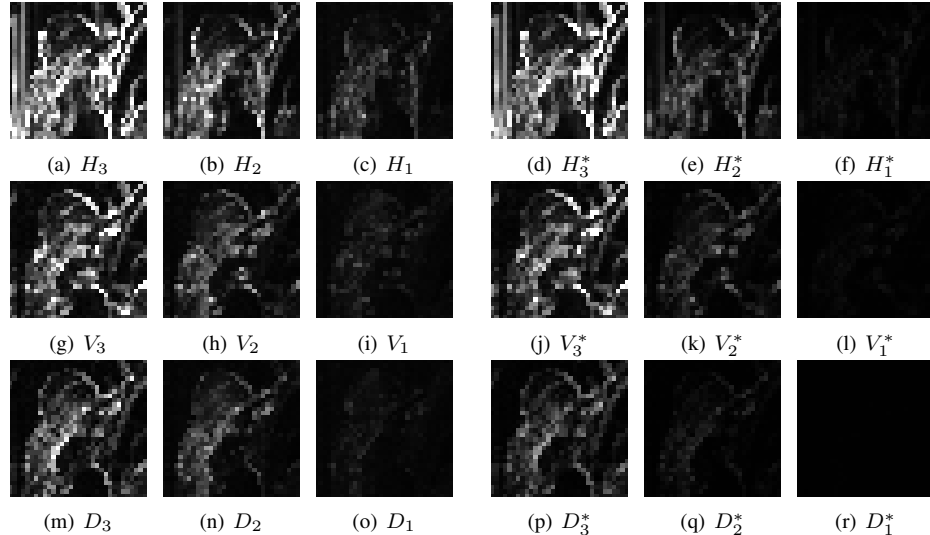


Fig. 2. Multiscale LMM maps for a sharp and blurred Lena image. For each image, a total of nine LMM maps are constructed, while H_i , V_i and D_i correspond to the sharp image and H_i^* , V_i^* and D_i^* correspond to the blurred one ($i = 1, 2, 3$).

B. Sharpness Ratios on LMM Maps

We here introduce a notation of sharpness ratio based on LMM maps. Let σ_L denotes the standard deviation of an LMM map L , $L \in \{H_i, V_i, D_i | i = 1, 2, 3\}$, a ratio $R(\sigma_{H_3}, \sigma_{H_2})$ is defined as follows:

$$R(\sigma_{H_3}, \sigma_{H_2}) = \frac{\sigma_{H_3}}{\sigma_{H_2} + \epsilon} \quad (1)$$

where a constant ϵ is added to avoid instability when σ_{H_2} is close to zero. To analyze its distribution, the ratio is computed over a large number of images. The first group of test images, having 3700 images, are taken from a public Micro image database [32]. These images are roughly chosen such that they are sharp and have no blurred areas due to lack of focus or motion. Fig. 3(a) plots the result of this group of images. It is seen that $R(\sigma_{H_3}, \sigma_{H_2})$ is typically in the range (1.6, 3.5). The second group comprises 145 Gaussian blur images of the LIVE database [33], where the blur level is determined by standard deviation σ_{blur} . Fig. 3(b) plots the results. We can see that the ratio $R(\sigma_{H_3}, \sigma_{H_2})$ increases with the amount of blur and is highly correlated with σ_{blur} .

Besides the ratio $R(\sigma_{H_3}, \sigma_{H_2})$, we find other three ratios, including $R(\sigma_{V_3}, \sigma_{V_2})$, $R(\sigma_{H_3}, \sigma_{H_1})$, and $R(\sigma_{V_3}, \sigma_{V_1})$, that have similar characteristics with respect to the effect blurring, as shown by Fig. 5¹. These four ratios, each of which is computed on LMM maps across different scales but in the same direction, are here referred as inter-scale sharpness (ISS) ratios. The ratios of $R(\sigma_{H_i}, \sigma_{D_i})$ and $R(\sigma_{V_i}, \sigma_{D_i})$, for $i = 2, 3$, also show similar statistical distributions as those of ISS ratios. As shown in Fig. 5, the distributions of the two ratios are closely correlated with the amount of blur. Similar plots can be obtained for the ratios $R(\sigma_{H_2}, \sigma_{D_2})$ and $R(\sigma_{V_2}, \sigma_{D_2})$. Each of the four ratios is computed on LMM maps within the same scale (*e.g.*, the 2-th or 3-th scale) but across different direction. We refer to them as inter-direction sharpness (IDS) ratios.

¹the plot of $R(\sigma_{V_3}, \sigma_{V_1})$ is similar to that of $R(\sigma_{H_3}, \sigma_{H_1})$ and is not shown here

The ISS and IDS ratios are effective in measuring image sharpness. The reasons for their effectiveness are analyzed here. One important characteristic of natural images is that their energy is mainly concentrated in lower-frequency coefficients and relative less energy is concentrated in higher-frequency coefficients [30], [34]. Subbands with more energy most often have a larger variance. When blur occurs, the edges and other details of an image bare smoothed. As a result, the energy of high-frequency components is often reduced more heavily than that of low-frequency components. Another important characteristic of natural images is that the different edges in space would lead to directional distributions of coefficients in blocks [35], [36]. Natural images typically have many horizontal and vertical edges [36], thus causing difference in the distribution of variance among LMM maps of the same scale. Because the distortion of blur has a heavier effect on subbands with smaller energy, the IDS ratios are likely to increase as the amount of blur increases. In fact, blur affect the perceptual quality of images at different scales and in different directions [26], [37]. The ISS and IDS ratios actually measure the effect of blur from a multiscale and a directional view. This has motivated us to combine ISS and IDS ratios for sharpness assessment.

C. Sharpness Ratios based Sharpness (SRS) Model

The use of ISS and IDS ratios that are computed on an entire LMM map for sharpness measurement would present a problem. If an input image has large smooth areas, the LMM maps of lower scales tend to have a very small variance, thus resulting in an incorrect prediction of sharpness. To solve this problem, the blocks that have strong edges or textures should be detected first, and then these should be used to compute the sharpness ratios. A block that has strong edges or textures here is referred as a high-activity block. In this section, we first present a method of high-activity block detection, and then introduce our sharpness ratios based measures.

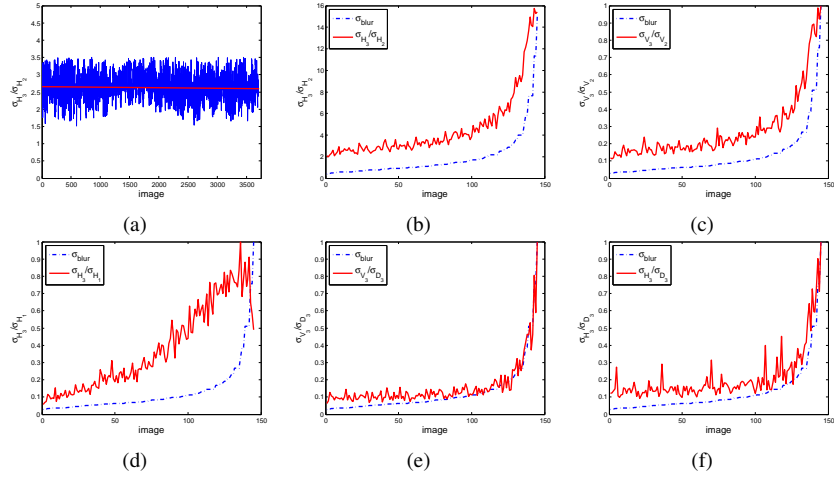


Fig. 3. Sharpness ratios of multiscale LMM maps.(a) the values of $R(\sigma_{H_3}, \sigma_{H_2})$ computed on 3700 images taken from the public database [32]. These images are chosen roughly to be sharp and have no blurred areas; (b) the values of $R(\sigma_{H_3}, \sigma_{H_2})$ over 145 Gaussian blur images of the LIVE database [33]. σ_{blur} denotes the level of Guassian blur. (c-f) the normalized values of $R(\sigma_{V_3}, \sigma_{V_2})$, $R(\sigma_{H_3}, \sigma_{H_1})$, $R(\sigma_{V_3}, \sigma_{D_3})$ and $R(\sigma_{H_3}, \sigma_{D_3})$ over the same set of LIVE blur images .

1) High-Activity-Block Detection: A block that has strong edges or textures generally has AC coefficients of large magnitudes. On the contrary, a smooth block typically has its energy concentrated on its DC coefficient, thus resulting in negligible energy compacted in some of its AC coefficients [30]. Based on this observation, the activity of a block can be computed as the ratio of the sum of all AC magnitudes to its DC magnitude. In this way, an activity map is obtained for the entire image. To avoid overestimation, those blocks whose DC coefficient is close to zero are neglected. Fig. 4(b) and Fig. 4(e) illustrates the activity maps of one original and its blurred image.

After the activity map is built, high-activity blocks can be detected. A block here is defined as a high-activity block if its activity value exceeds a certain threshold. Our method determines an appropriate threshold according to an activity-block detection rate r , which is estimated by the following equation:

$$r = r_0 + \xi \sigma_0 \quad (2)$$

where the constant parameters r_0 and σ_0 determines the range within which the detection rate can vary. Restricting the detection rate in a prior range is done to avoid instability caused by too low or too high a rate. ξ is a scalar weight ($0 < \xi < 1$) associated with image structure and blur level. For simplicity, we define ξ as a function of a log-energy index. It is observed that a higher level of image energy typically indicates a lower level of blur or a large amount of edges. We define a log-energy model in a similar way as the method [20]. Our method presents a similar but more simple and efficient way to compute the log-energy index. A energy map M is first obtained by:

$$M(k, l) = \sum_{i=1}^3 \pi_i (H_i(k, l) + V_i(k, l) + \lambda D_i(k, l)) \quad (3)$$

where the constant parameters π_i and λ are suggested to set as $\pi_i = 2^{3-i}$ and $\lambda = 8$, in order to give heavier weight to the subbands at the 1-th scale and the diagonal direction. This is because these subbands are regarded to have higher frequency

than other subbands [20]. With this energy map, the point that has maximum energy is selected. For each subband of the corresponding block, its log-energy is computed as:

$$E_s = \log \left(1 + \frac{1}{N_s} \sum_{(x,y) \in s} F^2(x, y) \right) \quad s \in \{h_i, v_i, d_i | i = 1, 2, 3\} \quad (4)$$

where N_s is the number of coefficients within the subband s , $F(x, y)$ denotes DCT coefficient at (x, y) . With these log-energy values, the total log-energy of the block is computed as:

$$\mathcal{M}_{lge} = \sum_{i=1}^3 \pi_i (E_{h_i} + E_{v_i} + \lambda E_{d_i}) \quad (5)$$

\mathcal{M}_{lge} is then taken as the log-energy measure of the whole image. Our method does not compute the log-energy for all blocks and is much more efficient. With the log-energy index, ξ is defined as

$$\xi = 1 - \exp \left(- \frac{\mathcal{M}_{lge}}{U} \right) \quad (6)$$

where U is a constant for normalization. In this manner, it allows more high-activity blocks to be detected if the blur level is lower, and induces a smaller detection rate if the blur level is higher. With the desired detection rate, the threshold is the activity value at the detection rate. Fig. 4(c) and Fig. 4(f) give the results of high-activity block detection for two images.

2) Sharpness Measures Using ISS and IDS Ratios: After detecting the high-activity blocks, our method locates in each LMM map a set of feature points, of which the indexes correspond to those detected blocks, and then computes ISS and IDS ratios on these sets of feature points. Let \tilde{R} denotes the value of R computed on the detected feature points, then a measure S_H is first built as:

$$S_H = (1 - \alpha) \tilde{R}(\sigma_{H_3}, \sigma_{H_2}) + \alpha \tilde{R}(\sigma_{H_3}, \sigma_{H_1}) \quad (7)$$

where the weight parameter α ($0 < \alpha < 1$) balances the effect of $\tilde{R}(\sigma_{H_3}, \sigma_{H_2})$ and $\tilde{R}(\sigma_{H_3}, \sigma_{H_1})$. S_H linearly combines the two horizontal ISS ratios and is an effective measure of

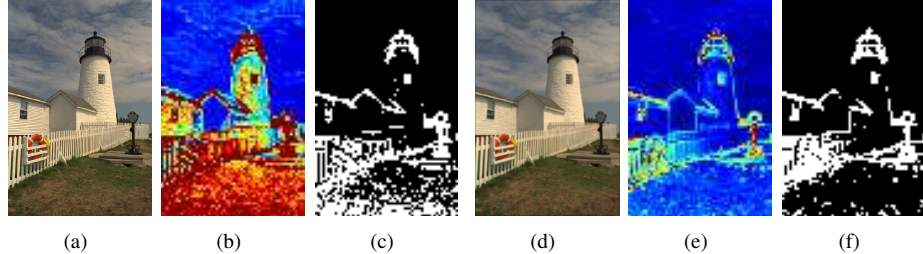


Fig. 4. (a) One original image taken from the LIVE database [33]; (b) The corresponding activity map, with activity values shown in colors ranging from blue (small value) to red (large value); (c) The result of high-activity block detection (white pixels denote detected blocks); (d) A blurred image with its corresponding activity map (e) and high-activity block detection result (f).

sharpness. An appropriate value of the weight parameter α is determined in our method via distribution analysis on the two ISS ratios. As seen in Fig. 5, the distributions of $R(\sigma_{H_3}, \sigma_{H_2})$ and $R(\sigma_{H_3}, \sigma_{H_1})$ both have close correlation with blur level. However, when blur reaches high levels, the distribution of $R(\sigma_{H_3}, \sigma_{H_1})$ may meet instability. In order to adjust the effect of $R(\sigma_{H_3}, \sigma_{H_2})$ and $R(\sigma_{H_3}, \sigma_{H_1})$, a lower weight should be used for the term $R(\sigma_{H_3}, \sigma_{H_1})$ when faster energy falloff happens in the lower scales. Let u_{L_i} denotes the average magnitude of the points in the whole LMM map L_i , $L_i \in \{H_i, V_i, D_i | i = 1, 2, 3\}$, the parameter α can be determined as:

$$\alpha = \frac{\pi_2(u_{H_2} + u_{V_2} + \lambda u_{D_2})}{\sum_{i=1}^2 \pi_i(u_{H_i} + u_{V_i} + \lambda u_{D_i})} \quad (8)$$

where the constant parameters λ and π_j are the same as those of Equ. 3. α is an index of relative amount of energy falloff across the 1-th and 2-th scale, while larger value indicates faster falloff energy occurs in the 1-th scale. We refer to α as scale weight. Another measure S_V can be defined in a similar way on two vertical ISS ratios:

$$S_V = (1 - \alpha)\tilde{R}(\sigma_{V_3}, \sigma_{V_2}) + \alpha\tilde{R}(\sigma_{V_3}, \sigma_{V_1}) \quad (9)$$

The same weight parameter is used because that the distributions of the two vertical ISS ratios are similar to those of the two horizontal ISS ratios.

With the four IDS ratios, two sharpness measures can also be built. Based on the IDS ratios of the second scale, one measure D_S is defined as:

$$D_S = (1 - \beta)\tilde{R}(\sigma_{H_2}, \sigma_{D_2}) + \beta\tilde{R}(\sigma_{V_2}, \sigma_{D_2}) \quad (10)$$

where β is a weight parameter ($0 < \beta < 1$). The two terms $\tilde{R}(\sigma_{H_2}, \sigma_{D_2})$ and $\tilde{R}(\sigma_{V_2}, \sigma_{D_2})$ capture the difference of energy concentration across directions along the 2-th scale. To well predict the perceptual sharpness, greater weight should be given to the directional term that has greater energy compaction. An appropriate value of the weight parameter β can be determined as:

$$\beta = \frac{\sum_{i=1}^3 \pi_i u_{V_i}}{\sum_{i=1}^3 \pi_i (u_{H_i} + u_{V_i})} \quad (11)$$

where π_i is defined in Equ. 3. The value of β given above can roughly quantify the differences in energy concentration across the horizontal and vertical directions. We refer β as

directional weight. Similarly, based on the ISS ratios of the third scale, another model D_T is defined as:

$$D_T = (1 - \beta)\tilde{R}(\sigma_{H_3}, \sigma_{D_3}) + \beta\tilde{R}(\sigma_{V_3}, \sigma_{D_3}) \quad (12)$$

Among the four measures presented above, S_H and S_V are defined across scales and capture energy falloff information along the horizontal and vertical directions, while D_S and D_T are defined across directions and capture energy compaction information along the second and third scales. These measures should be combined to induce a complete sharpness model. A scale-based model M_{sca} is first built by linearly combining S_H and S_V : $M_{sca} = (1 - \beta)S_H + \beta S_V$. Because the human visual system (HVS) is highly sensitive to the difference of orientation energy [26], the use of directional weight β would adaptively balance the effect of the two terms according to the amount of energy compaction on their associated direction. Another direction-based model M_{dir} is similarly built using the other two measures D_S and D_T : $M_{dir} = (1 - \alpha)D_S + \alpha D_T$. The use of scale weight α helps to normalize and adjust the two terms according to the ratio of energy falloff across scales. The two models M_{sca} and M_{dir} are then combined to form our sharpness ratios based sharpness (SRS) model:

$$M_{srs} = (1 - \xi)M_{sca} + \xi M_{dir} \quad (13)$$

where ξ is the factor based on the log-energy sharpness index. With $kappa$ as the weighting parameter, the measure prefers to put heavier weight on scale-based prediction M_{sca} when blur level getting higher. This is reasonable because the directional distribution of coefficients would be distorted by blur due to spatial edges are smoothed, thus resulting in less reliable prediction in M_{dir} .

D. Edge-Structure based Sharpness (ESS) Model

1) *The Model:* The work [23] proposed a method to estimate blurriness by exploiting the blur effect on the number of DCT edges. Inspired by this method, a similar model is presented in our method. The major difference is that our method introduces a new method of DCT edge extraction and an automatic method of setting the relevant thresholds. In our framework, an edge point $E_i(k, l)$ ($i = 1, 2, 3$) is defined as the directional local-maximum magnitude of a subband:

$$E_i(k, l) = \begin{cases} \max(h_i) & \text{if } d_h \geq d_v, d_h \geq d_d; \\ \max(v_i) & \text{if } d_v \geq d_h, d_v \geq d_d; \\ \max(d_i) & \text{if } d_d \geq d_h, d_d \geq d_v; \end{cases} \quad (14)$$

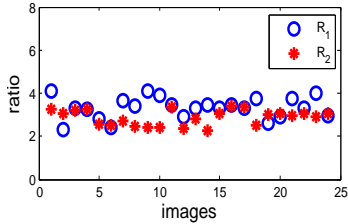


Fig. 5. The distributions of the ratios R_1 and R_2 over 24 LIVE original images [33]

where h_k , v_k and d_k ($k = 1, 2, 3$) are the corresponding subbands illustrated in Fig. 1, d_h is a horizontal energy index defined as $d_h = \sum_{k=2}^3 \sum_{F(i,j) \in h_k} |F(i,j)|$. d_v and d_d are indexes defined in a similar way for the vertical and diagonal direction. The reason for finding edge points using directional energy information is that coefficients tend to show directional distributions [36].

Blur would affect the number as well as the sharpness of the Roof-Structure (RS) and Gstep-Structure (GS) edges [18], [38] (these edges are referred as RGS edges). We extract RGS edges by a thresholding step using three thresholds T_i ($i = 1, 2, 3$) ($T_3 > T_2 > T_1$). For any point (k, l) , if any of the three edges $E_i(k, l)$ such that $E_i(k, l) > T_i$ and $E_1(k, l)$ is the smallest one, then (k, l) is taken as a RGS edge. When blur happens, the RGS edges would lose their sharpness. If a RGS edge such that $E_1(k, l) < T_1$, then it is a blurred RGS edge. Assuming the number of extracted RGS edges is N_s , and the number of blurred RGS edges is N_b , the ESS model is defined as:

$$\mathcal{M}_{ess} = \frac{N_b}{N_s + \epsilon} \quad (15)$$

where a positive constant ϵ is included to avoid dividing by zero. \mathcal{M}_{ess} forms an effective measure of sharpness, and is a factor of our sharpness model.

With the three DCT edge maps, we can also define a similar sharpness ratio based model because they are in different scales and shows similar characteristics as those of LMM maps. The difference is that here all the points of a whole edge map are used for sharpness ratio computation. This is because the edge points already represent the significant features of the image. This model referred as \mathcal{M}_{ers} is defined as:

$$\mathcal{M}_{ers} = (1 - \alpha)R(\sigma_{E_3}, \sigma_{E_2}) + \alpha R(\sigma_{E_3}, \sigma_{E_1}) \quad (16)$$

2) *Thresholding using Invariant Ratios*: The thresholds T_i ($i = 1, 2, 3$) determine the number of RGS edges to be found, and affect the effectiveness of this measure considerably. An automatic method of setting these thresholds is here established. Let u_{E_i} denotes the average magnitude of the largest 15th percentile edges in edge map E_i , this produces two ratios:

$$R_i = \frac{u_{E_{i+1}}}{u_{E_i}}, \quad i = 1, 2 \quad (17)$$

It is observed that, for high-quality natural images that have no blur distortion, these two ratios between scales are roughly invariant. Fig. 5 plots the two ratios computed over the original images of LIVE database. Note that 5 images among the total

29 original LIVE images are not used because they have out-of-focus blur areas. As shown, the values of the two ratios remain roughly constant, with R_1 typically within the range (1.6, 4.1) and R_2 within the range (1.8, 3.5). This can be also verified by a large number of other images. It is in fact consistent with the sharpness ratios on LMM maps which measures energy falloff across scales and directions. Then the relationship between the three thresholds can be modeled as follows:

$$T_{i+1} = K_i \xi^{\rho_i} T_i \quad i = 1, 2 \quad (18)$$

where K_i denotes the average value of R_i , and ρ_i is a constant weight parameter. In our experiments, K_i is set as the middle value in the corresponding range and we set $K_1 = K_2 = 2.85$. The term ξ^{ρ_i} is a scale factor that is associated with the normalized image log-energy ξ . An image with high log-energy generally tends to have strong edge structures or textures, thus the thresholds should be set to larger values accordingly. To this end, if T_1 is known, than T_2 and T_3 can be computed. The value of T_1 is determined as the r -th largest magnitude of the edge map E_1 , where r is the activity-block detection rate given by Equ. 2.

E. Blur Assessment Model

To this end, we combine the predefined models to induce an overall sharpness model. We refer our model as scale- and direction-based sharpness model (SDSM), which is given by:

$$\mathcal{M}_{sdsm} = \frac{1}{1 + \log(\mathcal{B} + 1)} \quad (19)$$

where

$$\mathcal{B} = \frac{\mathcal{M}_{srs}^\phi \mathcal{M}_{ess}^\varphi \mathcal{M}_{ers}^\gamma}{\mathcal{M}_{lge}^\eta + C} \quad (20)$$

where C is a constant to avoid instability. In all our experiments given in Sect. IV, the involved parameters in our SDSM model are set as $\phi = 0.3$, $\varphi = 0.5$, $\gamma = 0.1$, $\eta = 0.5$, $C = 1$, $r_0 = 0.15$ (Equ. 2), $\sigma_0 = 0.1$ (Equ. 2), $U = 20$ (Equ. 6), $\rho_1 = 0.7$ (Equ. 18) and $\rho_1 = 2.5$ (Equ. 18).

F. Local Blur Map Estimation

The above sections describe our method applied to the whole image for blur assessment at a global level. We can also apply it for local blur detection or local blur mapping problem. The goal of local blur mapping is to identify the blur level of every pixel in the image, resulting in a blur map that every pixel is labeled as either blurry or non-blurry.

To generate the local blur map, we compute inter-scale and inter-direction sharpness features corresponding to each overlapping 16×16 block of the image. The inter-scale and inter-direction sharpness feature is computed similarly as that described previously, but instead of using LMMs here we use the collections of corresponding coefficient subbands in each block. Similar as Fig. III-A, each subband is divided into small blocks of size 8×8 , 4×4 and 2×2 for levels 1, 2 and 3, respectively. The sum of absolute coefficient energy value is used for ratio computation, instead of using the standard deviation of each subband. The final metric of pixel-level sharpness is in a similar form as Equ. 13, where the weight parameter is computed in the local block manner.

IV. EXPERIMENTS

A. Blur Assessment Evaluation

In this section, we evaluate the performance of the proposed algorithm SDSM for NR image sharpness assessment. Our experiments employ blur image subsets from four public databases: LIVE [33], CSIQ [39], TID2008 [40] and TID2013 [41]. The number of Gaussian blur images in the four databases is 145, 150, 100 and 125 separately. For each blur image, both LIVE and CSIQ provide with differential mean opinion scores (DMOS), while TID2008 and TID2013 gives mean opinion scores (MOS). We compare our algorithm against a total of 11 relevant algorithms, including ARISM_c [24], S3 [5], LPC-SI [22], PSI [27], MLV [28], FISH_{bb} [20], RDCT [23], CPBD [12], JNB [10], BLIINDS2 [26], TLZZ [18].

In order to maximize correlation between objective metrics and subjective ground truth, a logistic function is often used to nonlinearly map between the predictions and the MOS or DMOS values. We adopt a 5-parameter nonlinear mapping function as suggested in [4], [42], which is given by:

$$f(x) = \tau_1 \left(\frac{1}{2} - \frac{1}{1 + \exp(\tau_2(x - \tau_3))} \right) + \tau_4 x + \tau_5 \quad (21)$$

where x and $f(x)$ denote the input prediction and the mapped score. The free parameters $\tau_i (i = 1, 2, 3, 4, 5)$ are estimated using a curve fitting operation. We use five criteria [12] to quantify the performance of these algorithms: (1) the Pearson linear correlation coefficient (PLCC), which measures the prediction accuracy; (2) the Spearman rank-order correlation coefficient (SRCC), which measures the prediction monotonicity; (3) the root mean squared error (RMSE), which quantify the prediction error; (4) the mean absolute error (MAE), which measures the absolute prediction error; and the outlier ratio (OR), which indicates the prediction consistency. A good metric should achieve high values in PLCC, SRCC, and low values in RMSE, MAE and OR.

Table I summarizes the performance results of these algorithms on the four databases. For each evaluation criterion, the top three best results are highlighted with boldface. To provide an overall comparison, Table II gives the average results for each metric over all four databases. The results of BLIINDS2 are not included for the LIVE database because BLIINDS2 uses LIVE for training. Hence the average results of BLIINDS2 are computed over other three databases. RMSE and MSE are not computed for BLIINDS2 because they should be computed over all four databases for fair comparison. It is observed that our SDSM model shows consistent and remarkably good performance over all four databases, and in general outperforms all other testing techniques.

Fig. 6 shows the scatter plots of objective predictions versus subjective scores, where the results of SDSM, ARISM_c, S3 and LPC-SI are plotted. It is seen that the proposed SDSM method generally achieves high quality predictions. For each database, the sample points of SDSM tend to be clustered closer to the diagonal line, which indicates perfect correlation between the predictions and the given scores. We also performed statistical significance analysis in order to provide

additional information regarding the relative performance of different image quality models [42]. This analysis is based on an assumption of Gaussianity of the residual differences between objective predictions (after the nonlinear mapping) and subjective scores. F-statistic can be used for comparing the variances of two sets of sample points, so as to judge whether they two sample sets come from the same distribution. As such, we can make a statistically sound judgment regarding the performance of the two methods in comparison. Table III gives the results of statistical significance of SSDM and other 11 metrics on the four public databases, wher “0” means that our SSDM model and the method of the corresponding column are statistically indistinguishable, and “+1” means the SSDM is statistically better than that of the corresponding column. It is seen that our model is statistically indistinguishable from ARISM_c [24] and S3 for LIVE, from PSI for TID2008, and ARISM_c [24], S3 and LPC-SI [22] for TID2013, and better than all other algorithms.

We have also compared the computational cost of our algorithm against that of ARISM_c [24] and S3. These two algorithms generally achieves most competitive performance on average over the four databases (See Table II). The test was conducted on a computer with Intel Core i7-5500U CPU at 2.40/2.39 GHz, 16 GB RAM and Window 8 64-bit. Fig. 7 gives the results. It is seen that our SSDM model is reasonable efficient. The majority cost of our method is in the block DCT. Since block DCT information is usually available for compressed video or image data and several fast techniques exist for DCT computation, our method would be made more faster for real time application.

B. Blur Mapping Evaluation

We compare our local blur mapping methods with several state-of-the-art methods [5], [43]–[48] using existing implementation. We evaluate these methods on a variety of images with different types and amount of blur provided in dataset [47]. In the generated blur mapps, the sharp regions have higher intensities than the blurred ones. The results are shown in Fig. 8. It can be seen that our proposed method can handle different blur types and shows strong discriminative ability on distinguishing between blurred and unblurred regions.

V. CONCLUSION

In this paper we present a new NR sharpness assessment algorithm that achieves remarkably high accuracy of prediction in an efficient manner. Our method is based on multiscale decomposition of non-overlapping blocks, and exploits statistical characteristics of the constructed LMM maps. With the detected high-activity blocks, a set of inter-scale and inter-direction sharpness ratios are found. These sharpness ratios predict image sharpness effectively from a multiscale and a directional view. They are linearly combined using automatically estimated weighting parameters to induce an overall effective sharpness model. To enhance accuracy, a sharpness factor based on the blur effect on DCT edges and a log-energy sharpness model are also incorporated into our

TABLE I
PERFORMANCE EVALUATIONS ON FOUR PUBLIC DATABASES.

| Database | Metrics | PLCC | SRCC | RMSE | MAE | OR |
|--------------|-------------------------|---------------|---------------|---------------|---------------|---------------|
| LIVE [33] | SDSM | 0.9730 | 0.9696 | 3.6320 | 2.8953 | 0 |
| | ARISM _c [24] | 0.9591 | 0.9566 | 4.4513 | 3.5935 | 0 |
| | S3 [5] | 0.9527 | 0.9394 | 4.7773 | 3.7099 | 0.0069 |
| | LPC-SI [22] | 0.9317 | 0.9411 | 5.7095 | 4.4664 | 0.0483 |
| | PSI [27] | 0.9474 | 0.9387 | 5.0322 | 4.0076 | 0.0071 |
| | MLV [28] | 0.9052 | 0.9315 | 6.6831 | 5.2769 | 0.0828 |
| | FISH _{bb} [20] | 0.9316 | 0.9380 | 5.7133 | 4.5608 | 0.0069 |
| | RDCT [23] | 0.9438 | 0.9357 | 5.1952 | 4.2638 | 0.0138 |
| | CPBD [12] | 0.9125 | 0.9190 | 6.4313 | 4.7350 | 0.0483 |
| | JNB [10] | 0.8189 | 0.7877 | 9.0236 | 6.8430 | 0.1517 |
| | BLIINDS2 [26] | - | - | - | - | - |
| | TLZZ [18] | 0.8136 | 0.8431 | 9.1408 | 7.1576 | 0.1517 |
| CSIQ [39] | SDSM | 0.9574 | 0.9304 | 0.0827 | 0.0650 | 0.1733 |
| | ARISM _c [24] | 0.8885 | 0.9314 | 0.1315 | 0.1004 | 0.3400 |
| | S3 [5] | 0.9175 | 0.9059 | 0.1140 | 0.0887 | 0.2933 |
| | LPC-SI [22] | 0.9097 | 0.9071 | 0.1190 | 0.0982 | 0.3067 |
| | PSI [27] | 0.9428 | 0.9117 | 0.0955 | 0.0748 | 0.2133 |
| | MLV [28] | 0.8922 | 0.9248 | 0.1294 | 0.1030 | 0.3333 |
| | FISH _{bb} [20] | 0.9284 | 0.9195 | 0.1065 | 0.0848 | 0.2667 |
| | RDCT [23] | 0.9258 | 0.8842 | 0.1084 | 0.0858 | 0.2733 |
| | CPBD [12] | 0.8834 | 0.8853 | 0.1346 | 0.1083 | 0.3460 |
| | JNB [10] | 0.7902 | 0.8382 | 0.1753 | 0.1432 | 0.3729 |
| | BLIINDS2 [26] | 0.8676 | 0.8766 | 0.1425 | 0.1139 | 0.3267 |
| | TLZZ [18] | 0.8937 | 0.8604 | 0.1286 | 0.1043 | 0.3000 |
| TID2008 [40] | SDSM | 0.8892 | 0.8879 | 0.5370 | 0.4085 | 0.5800 |
| | ARISM _c [24] | 0.8544 | 0.8679 | 0.6097 | 0.4801 | 0.6500 |
| | S3 [5] | 0.8542 | 0.8460 | 0.6102 | 0.4730 | 0.7300 |
| | LPC-SI [22] | 0.8587 | 0.8699 | 0.6013 | 0.4820 | 0.7100 |
| | PSI [27] | 0.8529 | 0.8454 | 0.6126 | 0.4911 | 0.6900 |
| | MLV [28] | 0.8593 | 0.8546 | 0.6003 | 0.4658 | 0.6800 |
| | FISH _{bb} [20] | 0.8459 | 0.8486 | 0.6192 | 0.4746 | 0.6800 |
| | RDCT [23] | 0.8623 | 0.8544 | 0.5943 | 0.4720 | 0.7300 |
| | CPBD [12] | 0.8331 | 0.8412 | 0.6492 | 0.4917 | 0.6600 |
| | JNB [10] | 0.6777 | 0.6667 | 0.8639 | 0.6601 | 0.7500 |
| | BLIINDS2 [26] | 0.8267 | 0.8210 | 0.6603 | 0.5340 | 0.7100 |
| | TLZZ [18] | 0.6827 | 0.7233 | 0.8575 | 0.7007 | 0.8400 |
| TID2013 [41] | SDSM | 0.9060 | 0.8922 | 0.5283 | 0.4134 | 0.6240 |
| | ARISM _c [24] | 0.8980 | 0.9016 | 0.5492 | 0.4424 | 0.6800 |
| | S3 [5] | 0.8816 | 0.8609 | 0.5891 | 0.4747 | 0.7280 |
| | LPC-SI [22] | 0.8940 | 0.8888 | 0.5591 | 0.4585 | 0.7280 |
| | PSI [27] | 0.8793 | 0.8680 | 0.5944 | 0.4894 | 0.7360 |
| | MLV [28] | 0.8829 | 0.8785 | 0.5859 | 0.4581 | 0.6560 |
| | FISH _{bb} [20] | 0.8673 | 0.8598 | 0.6212 | 0.5032 | 0.7280 |
| | RDCT [23] | 0.8739 | 0.8662 | 0.6099 | 0.4917 | 0.7040 |
| | CPBD [12] | 0.8620 | 0.8518 | 0.6325 | 0.5111 | 0.7040 |
| | JNB [10] | 0.6929 | 0.6902 | 0.9004 | 0.6964 | 0.7840 |
| | BLIINDS2 [26] | 0.8492 | 0.8351 | 0.6589 | 0.5103 | 0.6900 |
| | TLZZ [18] | 0.7010 | 0.7071 | 0.8900 | 0.7237 | 0.8320 |

method. Experiments on a large number of public images with provided subjective scores have shown that the proposed SDSM metric is highly correlated with human perceptual of image sharpness, and outperforms the current state-of-the-art techniques. For future work, the performance of SDSM model on noisy images will be tested and improved.

APPENDIX A PROOF OF THE FIRST ZONKLAR EQUATION

Appendix one text goes here.

APPENDIX B

Appendix two text goes here.

ACKNOWLEDGMENT

The authors would like to thank...

REFERENCES

- [1] K. Gu, G. Zhai, X. Yang, W. Zhang, and C. W. Chen, "Automatic contrast enhancement technology with saliency preservation," *IEEE Transactions on Circuits and Systems for Video Technology*, vol. 18, no. 9, pp. 1237–1246, 2014.

TABLE II
AVERAGE RESULTS OVER ALL FOUR PUBLIC DATABASES.

| Metrics | PLCC | SRCC | RMSE | MAE | OR |
|-------------------------|---------------|---------------|---------------|---------------|---------------|
| SDSM | 0.9314 | 0.9200 | 1.1950 | 0.9456 | 0.3443 |
| ARISM _c [24] | 0.9000 | 0.9144 | 1.4354 | 1.1541 | 0.4375 |
| S3 [5] | 0.9015 | 0.8892 | 1.5226 | 1.1866 | 0.4196 |
| LPC-SI [22] | 0.8985 | 0.9013 | 1.7472 | 1.3763 | 0.4482 |
| PSI [27] | 0.9056 | 0.8910 | 1.5837 | 1.2657 | 0.4116 |
| MLV [28] | 0.8849 | 0.8973 | 1.9997 | 1.5759 | 0.4380 |
| FISH _{bb} [20] | 0.8942 | 0.8915 | 1.7651 | 1.4058 | 0.4204 |
| RDCT [23] | 0.9014 | 0.8851 | 1.6261 | 1.3283 | 0.4303 |
| CPBD [12] | 0.8727 | 0.8743 | 1.9684 | 1.4669 | 0.4481 |
| JNB [10] | 0.7449 | 0.7457 | 2.1382 | 2.1063 | 0.5631 |
| BLIINDS2 [26] | 0.8478 | 0.8442 | - | - | 0.5722 |
| TLZZ [18] | 0.7728 | 0.7834 | 2.7542 | 2.1715 | 0.5309 |

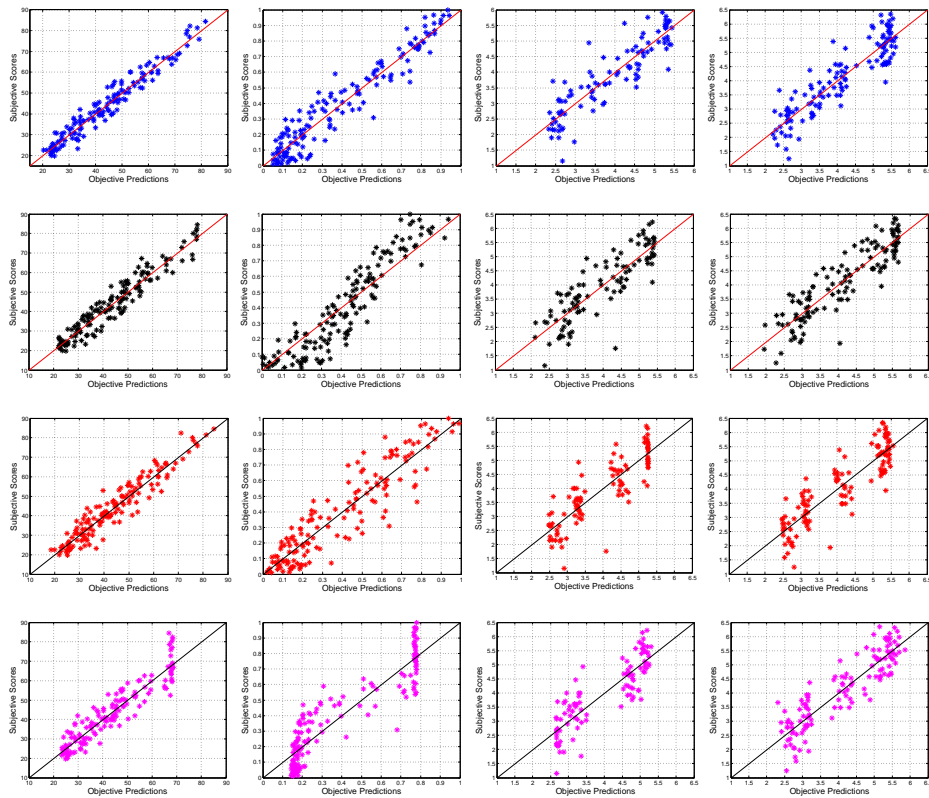


Fig. 6. Scatter plots between the subjective scores and the objective predictions of SDSM (Top row), ARISM_c [24] (Second row), S3 [5] (Third row) and LPC-SI [22] (Bottom row) on the four databases. From left to right, the columns correspond to LIVE [33], CSIQ [39], TID2008 [40] and TID2013 [41] databases.

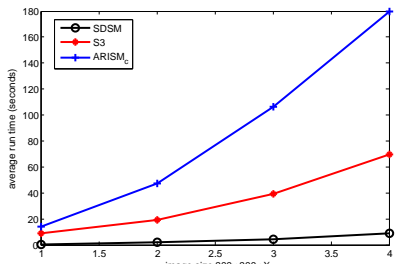


Fig. 7. Average running time of SDSM, S3 [5] and ARISM_c [24]

- [2] X. Zhu and P. Milanfar, "Automatic parameter selection for denoising algorithms using a no-reference measure of image content," *IEEE Transactions on Image Processing*, vol. 19, pp. 3116–3132, 2010.

- [3] N. Joshi, C. L. Zitnick, R. Szeliski, and D. J. Kriegman, "Image deblurring and denoising using color priors," in *IEEE International Conference on Computer Vision and Pattern Recognition*, 2009.
- [4] A. Ciancio, A. L. N. T. da Costa, and E. A. B. da Silva, "No-reference blur assessment of digital pictures based on multifeature classifiers," *IEEE Transactions on Image Processing*, vol. 20, no. 1, pp. 64–75, 2011.
- [5] C. T. Vu, T. D. Phan, and D. M. Chandler, "S3: A spectral and spatial measure of local perceived sharpness in natural images," *IEEE Transactions on Image Processing*, vol. 21, pp. 934–945, 2011.
- [6] P. Marziliano, F. Dufaux, S. Winkler, and T. Ebrahimi, "Perceptual blur and ringing metrics application to jpeg2000," *Signal Processing: Image Communication*, vol. 19, pp. 163–172, 2004.
- [7] S. Varadarajan and L. J.Karam, "An improved perception-based no-reference objective image sharpness metric using iterative edge refinement," in *IEEE International Conference on Image Processing*, 2008.
- [8] Y. C. Chung, J. M. Wang, R. R.Bailey, S. W. Chen, and S. lih Chang, "A non-parametric blur measure based on edge analysis for

TABLE III

STATISTICAL SIGNIFICANCE COMPARISON OF SDSM AND OTHER 11 METRICS. THE NUMBER 1 TO 11 SEPARATELY DENOTES THE METHOD ARISM_c [24], S3 [5], LPC-SI [22], PSI [27], MLV [28], FISH_{bb} [20], RDCT [23], CPBD [12], JNB [10], BLIINDS2 [26], AND TLZZ [18].

| | 1 | 2 | 3 | 4 | 5 | 6 | 7 | 8 | 9 | 10 | 11 |
|---------|----|----|----|----|----|----|----|----|----|----|----|
| LIVE | 0 | 0 | +1 | +1 | +1 | +1 | +1 | +1 | +1 | +1 | +1 |
| CSIQ | +1 | +1 | +1 | 0 | +1 | +1 | +1 | +1 | +1 | +1 | +1 |
| TID2008 | +1 | +1 | +1 | +1 | +1 | +1 | +1 | +1 | +1 | +1 | +1 |
| TID2013 | 0 | 0 | 0 | +1 | +1 | +1 | +1 | +1 | +1 | +1 | +1 |

- image processing applications," in *IEEE Conference on Cybernetics and Intelligent Systems*, 2014.
- [9] L. Liang, J. Chen, S. Ma, D. Zhao, and W. Gao, "A no-reference perceptual blur metric using histogram of gradient profile sharpness," in *IEEE International Conference on Image Processing*, 2009.
 - [10] R. Ferzli and L. J. Karam, "A no-reference objective image sharpness metric based on the notion of just noticeable blur," *IEEE Transactions on image processing*, vol. 18, no. 4, pp. 717–728, 2009.
 - [11] N. G. Sadaka, L. J. Karam, R. Ferzli, and G. P. Abousleman, "A no-reference perceptual image sharpness metric based on saliency-weighted foveal pooling," in *IEEE International Conference on Image Processing*, 2008.
 - [12] N. D. Narvekar and L. J. Karam, "A no-reference image blur metric based on the cumulative probability of blur detection," *IEEE Transactions on Image Processing*, vol. 20, no. 9, pp. 2678–2683, 2011.
 - [13] D. J. Field and N. Brady, "Visual sensitivity, blur and the sources of variability in the amplitude spectra of natural scenes," *Vis. Res.*, vol. 37, no. 23, pp. 3367–3383, 1997.
 - [14] X. Marichal, W.-Y. Ma, and H. Zhang, "Blur determination in the compressed domain using dct information," in *IEEE International Conference on Image Processing*, 1999.
 - [15] J. Caviedes and F. Oberti, "A new sharpness metric based on local kurtosis, edge and energy information," *Signal Processing: Image Communication*, vol. 19, pp. 147–161, 2004.
 - [16] D. Shaked and I. Tastl, "Sharpness measure: Towards automatic image enhancement," in *IEEE International Conference on Image Processing*, 2005.
 - [17] R. Ferzli and L. J. Karam, "No-reference objective wavelet based noise immune image sharpness metric," in *IEEE International Conference on Image Processing*, 2005.
 - [18] H. Tong, M. Li, H. Zhang, and C. Zhang, "Blur detection for digital images using wavelet transform," in *IEEE International Conference on Multimedia and Expo*, 2004.
 - [19] M.-J. Chen and A. C. Bovik, "No-reference image blur assessment using multiscale gradient," *EURASIP Journal on Image and Video Processing*, vol. 1, no. 3, 2011.
 - [20] P. VVu and D. M.Chandler, "A fast wavelet-based algorithm for global and local image sharpness estimation," *Signal Processing Letters*, vol. 19, pp. 423–426, 2012.
 - [21] R. Hassen, Z. Wang, and M. Salama, "No-reference image sharpness assessment based on local phase coherence measurement," in *IEEE International conference on acoustics, speech and signal processing*, 2010.
 - [22] R. Hassen, Z. Wang, and M. M.A.Salama, "Image sharpness assessment based on local phase coherence," *IEEE Transactions on Image Processing*, vol. 22, no. 7, pp. 2798–2810, 2013.
 - [23] Z. Zhang, Y. Liu, X. Tan, and M. Zhang, "Robust sharpness metrics using reorganized dct coefficients for auto-focus application," in *Asian Conference on Computer Vision*, 2014.
 - [24] K. Gu, G. Zhai, W. Lin, X. Yang, and W. Zhang, "No-reference image sharpness assessment in autoregressive parameter space," *IEEE Transactions on Image Processing*, vol. 24, no. 10, pp. 3218–3231, 2015.
 - [25] M. A.Saad, A. C. Bovik, and C. Charrier, "A dct statistics-based blind image quality index," *IEEE Signal Processing Letters*, vol. 17, no. 6, pp. 583–586, 2008.
 - [26] M.Saad, A.Bovik, and C.Charrier, "Blind image quality assessment:a natural scene statistics approach in the dct domain." *IEEE Transactions on Image Processing*, vol. 21, pp. 3339–3352, 2012.
 - [27] C. Feichtenhofer, H. Fassold, and P. Schallauer, "A perceptual image sharpness metric based on local edge gradient analysis," *IEEE Signal Processing Letters*, vol. 20, pp. 379–382, 2013.
 - [28] K. Bahrami and A. C. Kot, "A fast approach for no-reference image sharpness assessment based on maximum local variation," *IEEE Signal Processing Letters*, vol. 21, no. 6, pp. 751–755, 2014.
 - [29] Z. Xiong, O. Guleryuz, and M. T. Orchard, "A dct-based embedded image coder," *Signal Processing Letters*, vol. 3, no. 11, pp. 289–290, 1996.
 - [30] D. Zhao, W. Gao, and Y. K. Chan, "Morphological representation of dct coefficients for image compression," *IEEE Transactions on Circuits and Systems for Video Technology*, vol. 12, no. 9, pp. 819–823, 2002.
 - [31] L. Ma, S. Li, F. Zhang, and K. N. Ngan, "Reduced-reference image quality assessment using reorganized dct-based image representation," *IEEE Transactions on Multimedia*, vol. 13, no. 4, pp. 824–829, 2011.
 - [32] A. Criminisi, P. Kohli, T. Minka, C. Rother, T. Sharp, J. Shotton, and J. Winn, "Microsoft research cambridge object recognition image database," <http://research.microsoft.com/en-us/projects/objectclassrecognition/default.aspx>.
 - [33] H. R. Sheikh, Z. Wang, L. Cormack, and A. C. Bovik, "Live image quality assessment database release 2," <http://live.ece.utexas.edu/research/quality>.
 - [34] E. Y. Lam and J. W. Goodman, "A mathematical analysis of the dct coefficient distributions for images," *IEEE Transactions on Image Processing*, vol. 9, no. 10, pp. 1661–1666, 2000.
 - [35] J.Y.Nam and K.R.Rao, "Image coding using a classified dct/vq based on two-channel conjugate vector quantization," *IEEE Trans. Circuits Syst. Video Technol.*, vol. 1, no. 4, pp. 325–336, 1991.
 - [36] B. Zeng and J. Fu, "Directional discrete cosine transforms a new framework for image coding," *IEEE Trans. Circuits Syst. Video Technol.*, vol. 18, no. 3, pp. 305–313, 2008.
 - [37] X. Gao, W. Lu, D. Tao, and X. Li, "Image quality assessment based on multiscale geometric analysis," *IEEE Transactions on Image Processing*, vol. 18, pp. 1409–1423, 2009.
 - [38] Y. Y. Tang, L. Yang, and J. Liu, "Characterization of dirac-structure edges with wavelet transform," *IEEE Transactions on Systems, Man, And Cybernetics - Part B: Cybernetics*, vol. 30, no. 1, pp. 93–109, 2000.
 - [39] E.C.Larson and D.M.Chandler, "Most apparent distortion: full-reference image quality assessment and the role of strategy," *Journal of Electronic Imaging*, vol. 19, no. 1, 2010.
 - [40] N.Ponomarenko, V.Lukin, A.Zelensky, K.Egiazarian, M.Carli, and F.Battisti, "Tid2008- a database for evaluation of full-reference visual quality assessment metrics," *Advances of Modern Radioelectronics*, vol. 10, 2009.
 - [41] N. Ponomarenko, O. Ieremeiev, V. Lukin, K. Egiazarian, L. Jin, J. Astola, B. Vozel, K. Chehdi, M. Carli, F. Battisti, and C.-C. J. Kuo, "Color image database tid2013: Peculiarities and preliminary results," in *Proceedings of 4th European Workshop on Visual Information Processing*, 2013.
 - [42] H. R. Sheikh, M. F. Sabir, and A. C. Bovik, "A statistical evaluation of recent full reference image quality assessment algorithms," *IEEE Transactions on Image Processing*, vol. 15, pp. 3441–3452, 2006.
 - [43] C. Tand, J. Wu, Y. Hou, P. Wang, and W. Li, "A spectral and spatial approach of coarse-to-fine blurred image region detection," *IEEE Signal Processing Letters*, vol. 23, no. 11, pp. 1652–1656, 2016.
 - [44] A. Chakrabarti, T. Zickler, and W. T. Freeman, "Analyzing spatially-varying blur," in *CVPR*, 2010.
 - [45] B. su, shijian lu, and chew lim tan, "Blurred image region detection and classification," in *ACM MM*, 2011.
 - [46] X. Yi and M. Eramian, "Lbp-based segmentation of defocus blur," *IEEE Transactions on image processing*, vol. 25, no. 4, pp. 1626–1638, 2016.
 - [47] J. Shi, L. Xu, and J. Jia, "Discriminative blur detection features," in *CVPR*, 2014.
 - [48] S. A. Golestaneh and L. J. Karam, "Spatially-varying blur detection based on multiscale fused and sorted transform coefficients of gradient magnitudes," in *CVPR*, 2017.

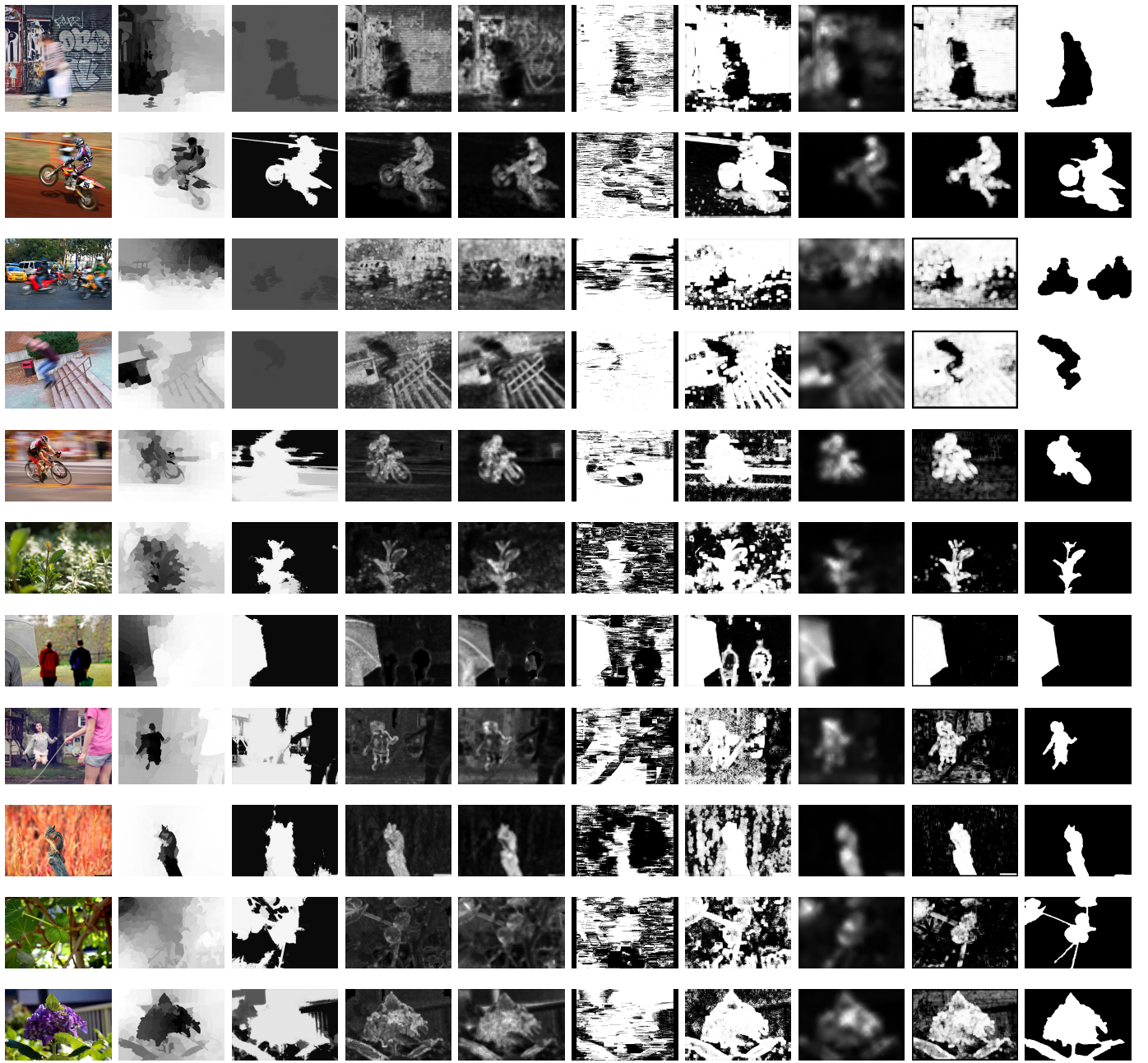


Fig. 8. Comparision results on images selected from [47] for several state-of-the-art algorithms. From left to right, the methods compared are [43], [46], [5], [45], [44], [47], [48] and ours. The last column gives the ground truth of binary blur maps.

Defense Technology, China, in 2007, and obtained his Ph.D. degree in computer engineering from Nanyang Technological University, Singapore, in 2013. He is currently a Lecturer in the Department of System Engineering, National University of Defense Technology. His research interests include image processing and computer vision.

Xinhua Xiao received the B.S. degree in automation from the University of Electronic Science and Technology of China, Chengdu, China, in 2012, and the M.S. degree in system engineering from the National University of Defense Technology, Changsha, China, in 2015. He is currently working toward the Ph.D. degree in system engineering from the National University of Defense Technology. He was the recipient of the winner prize of object localization task in ILSVRC 2017. His current research interests include saliency detection and image/video object.

Hanlin Tan obtained his Bachelor's degree in National University of Defense Technology, Changsha, China, in the year 2014. He started to work for PhD degree ahead of schedule in the year 2016. Currently he is a PhD Candidate at the College of Information System and Management, National University of Defense Technology. His research interests include computer vision, image processing, and machine learning.

Liu Yu received his B.S. degree from Northwestern Polytechnical University, Xi'an, China in 2005. He then received his MSc on image processing and Ph.D. on computer graphics from the University of East Anglia, Norwich, UK, in 2007 and 2011, respectively. He is currently an Associate Professor in the Department of System Engineering, NUDT. His research interests include image/video processing, computer graphics, and visual haptic technology.

Zhang Maojun received his B.S. and Ph.D. degrees in system engineering from National University of Defense Technology, Changsha, China, in 1992 and 1997, respectively. He is currently a full Professor of National University of Defense Technology (NUDT), and is the Director of the Department of System Engineering of NUDT. He is the author or coauthor of more than 50 published papers and technical reports. His research interests include virtual reality and image processing technology.